# AN ARRAY OF WIDE-FIELD TELESCOPES IN SICILY FOR NEOs AND SPACE DEBRIS MONITORING: INTRODUCTION AND FIRST RESULTS

**A. Nastasi [(1,3)], A. Rossi [(2)], G. Micela [(3)], G. B. Valsecchi [(4,2)], A. Di Cecco [(5)], M. Castronuovo [(5)]**

*[(1)] GAL Hassin – Centro Internazionale per le Scienze Astronomiche, Via della Fontana Mitri 3, 90010 Isnello (Italy), Email: alessandro.nastasi@galhassin.it*

*[(2)] IFAC-CNR, Via Madonna del Piano 10, Sesto Fiorentino (Italy), Email: a.rossi@ifac.cnr.it*

*[(3)] INAF - Osservatorio Astronomico di Palermo, Piazza del Parlamento 1, 90134 Palermo (Italy), Email: giusi@astropa.inaf.it*

*[(4)] IAPS-INAF, via Fosso del Cavaliere 100, 00133 Roma (Italy), Email: giovanni@iaps.inaf.it*

*[(5)] Italian Space Agency (ASI), via del Politecnico snc, Rome 00133 I (Italy), Email: {alessandra.dicecco, marco.castronuovo}@asi.it*

## ABSTRACT

Here we present new wide-field telescopes that are being installed in the central North part of Sicily (Italy). This installation is motivated both by the extremely good sky and geographical conditions of the area and by the observational infrastructures and capabilities already provided by the nearby "GAL Hassin" astronomical center. This work will especially focus on the results of a pilot study run between July and December 2022 with the 0.4 m aperture, fast (f/D = 3.8) Galhassin Robotic Telescope 1 (GRT1), on the photometric characterization of 16 artificial satellites and space debris with different sizes and altitudes down to 500 km. These results validate the high accuracy in photometry, position and time achieved by means of our facility and pave the way to the 1-m class Wide-field Mufara Telescope (WMT) and the upcoming ESA survey NEOSTEL (Flyeye) telescope.

## 1 INTRODUCTION

Wide-field and fast telescopes are key facilities to discover, monitor and characterize rapid-moving objects in the sky, such as Near Earth Objects (NEOs) and space debris. When used in combination, the strengths and weaknesses of the individual facilities can be respectively enforced and compensated in order to reach a higher effectiveness for the detection and accurate physical characterization of rapid-moving targets. An array of two wide field telescopes is currently under construction in the North central part of Sicily, within the Madonie Natural Park, which is characterized by low level of light pollution, favourable weather conditions and a low-latitude location, enabling the observations of the sky down to DEC ~ -35° [1]. For this reason, this area has been selected as the designated site for the future ESA survey NEOSTEL (a.k.a. "Flyeye") telescope [2, 3], to be installed on the 1865 m high peak of Mount Mufara (Lat = 37°52′07.9″N, Lon = 14°01′12.6″E). In addition, since the end of 2020 the same mountain already hosts the Wide-field Mufara Telescope (WMT – Fig. 1), a 1 m f/D = 2.1 prime focus telescope built by OfficinaStellare S.p.A. [4]. This telescope has a 2.5 × 2.5 deg field of view (FoV) and will reach a limiting magnitude of V = 21.5 with 60 sec exposure time. Unlike the Flyeye, the WMT will be equipped with four *griz* 2nd generation Sloan filters, key to perform complementary physical characterizations of fast targets which might be simultaneously observed by the ESA NEOSTEL in wide visible band. The WMT is currently under the commissioning phase and it is expected to get fully operational by Spring 2023. Once active, the WMT will be fully remotely controlled and handled by and from the GAL Hassin astronomical center located in Isnello (near Palermo), 10 km away from Mount Mufara. The GAL Hassin was inaugurated in 2016 and is equipped with several facilities for its astronomical outreach, educational and research activities. Among them, it hosts the Galhassin Robotic Telescope 1 (GRT1 – Lat = 37°56′21.8″N, Lon = 14°01′14.2″E, Alt = 610 m), an OfficinaStellare Ritchey-Chrétien telescope with an aperture of 0.4 m, a focal ratio of f/D = 3.8 and a field of view of 1.2 × 1.2 deg (Fig. 2). In order to test the capabilities and the limits of the GRT1 in observing fast-

*Figure 1. The Wide-field Mufara Telescope (WMT) installed on Mount Mufara, Sicily.*

*Proc. 2nd NEO and Debris Detection Conference, Darmstadt, Germany, 24-26 January 2023, published by the ESA Space Safety Programme Office Ed. T. Flohrer, R. Moissl, F. Schmitz (http://conference.sdo.esoc.esa.int, February 2023)*

moving artificial objects and check various observational strategies which may be implemented on that category of targets by the aforementioned upcoming 1-m class telescopes, an observational test campaign was run with the GRT1 on July, August and December 2022. The results obtained from these observations specifically addressed the following points:

- Testing of methods and software tools used to point and track artificial targets moving at different rates (Sect. 4).
- Estimating lightcurves sampling frequency when observing with single or alternating filters (Sect. 2).
- Testing of methods to correct the observed instrumental magnitudes for atmospheric extinction and change of distance from the observer (Sect. 3).
- Estimate the photometric accuracy with spherical, non-intrinsically variable satellites (Sect. 4.1).
- Verify the consistency of the photometric results achieved on the same target when tracked at different rates (Sect. 4.2).
- Validate the possibility to observe *decaying* debris in order to measure their astrometry and characterize their multi band photometry (Sect. 4.5).
- Perform multi-band characterization of rotating objects and correlation of the measured colours with the rotation phase (Sect. 4.4, 4.5).
- Estimate the accuracy in the recorded timing and hence of the astrometric measurements (Sect. 5).
- Measure the *gri* photometric properties of global navigation satellite system (GNSS) satellites, and if satellites of the same constellation may appear to have a same "typical colour" (Sect. 5).

In Sect. 2 we provide the technical characteristics of the GRT1 telescope. Sect. 3 describes the motivation and strategies adopted for the targets selection and their main properties, as well as the software and methods used for the data analysis. Sect. 4 details the main results found for the targets observed in summer 2022. In Sect. 5 we describe the *gri* observations of 9 satellites of different GNSS constellations, run on Dec. 21$^{st}$, and the results we obtained. Finally, in Sect. 6 we summarize our findings.

## 2 The GRT1 observatory

The GRT1 mounts a Finger Lake Instruments (FLI) ProLine 16803 CCD camera, a 10-slots FLI filter wheel, including four *ugri* 2nd generation Sloan photometric set, and it is moved by a 10Micron GM3000 HPS mount. The observatory is installed within a 3M V3 ScopeDome. Overall, such a setting allows the GRT1 to follow any target either at sidereal or custom tracking rate, up to 2 deg/sec, and to take consecutive images with *alternating* filters. The latter option is especially suited for performing *almost simultaneous* multiband photometry of space objects, with time gaps between consecutive filters of 3.5 seconds, and between two consecutive sets

*Figure 2. The Galhassin Robotic Telescope 1 (GRT1), hosted within the GAL Hassin astronomical center.*

of multiband frames of 11 seconds. Since 2019 the GRT1 is being intensively used for the detection, confirmation and physical characterization of solar system minor bodies, with Minor Planet Center (MPC) code L34. To date, L34 has reported to MPC astrometry of more than 200 NEOs up to rate of 15 deg/h, with a median residual of $\chi \sim 0.73$ (as reported by NEODyS-2: https://newton.spacedys.com/neodys). The high astrometric accuracy of the GRT1 is achieved not only via its large FoV and sensitivity (which both guarantee to have more stars for a robust astrometric reference), but also by its *accurate time recording* enabled through a GPS synchronization facility which keeps the clock of the controlling PC constantly synchronized to the UTC time within 2 ms. By considering also internal delays due to software response and camera shutter activation, we could verify that the overall timing accuracy achieved by the GRT1 amounts to about *0.1 sec*. Such an important bias can be estimated (and hence corrected) by measuring the astrometry of GNSS satellites, as discussed in Sect. 5

## 3 Observational strategy and data analysis

The summer session of the GRT1 pilot campaign targeted a total of 7 objects, whose properties are listed in Tab. 1.

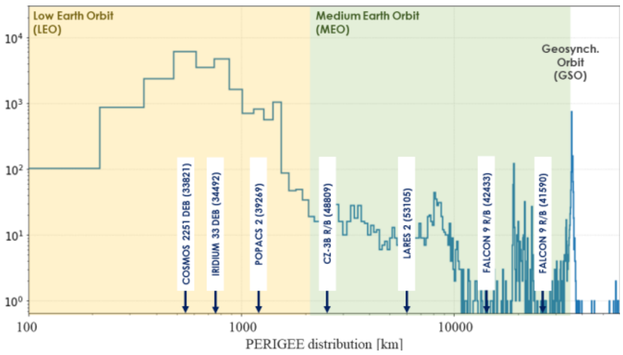


*Figure 3. Position on the perigee distribution of the 7 targets observed by the GRT1 during its summer 2022 test campaign. The underlying histogram shows the current distribution of all satellites and debris.*

Table 1 – Properties of the 7 objects observed during the Summer 2022 session of the GRT1 pilot campaign, sorted by decreasing altitude. Radar Cross Section (*RCS*) is a measure of the object size. Specifically, for RCS < 0.1 $m^2$ the object is classified as "Small"; for 0.1 < RCS/$m^2$ < 1.0 the object size is classified as "Medium"; for 1.0 $m^2$ < RCS the object size is classified as "Large". *Obs. Altitude* refers to the median altitude of the target during the reported observation time. *ΔRange* reports the variation of the distance from the observer between the first and last observation. Negative values indicate the object was *approaching* the observer. For objects LARES 2, POPACS 2 and CZ-3B DEB, *ΔRange* is the difference between the maximum and minimum range values, as the latter occurred around the observation mid-time, in correspondence of the maximum elevation. *Elevation* indicates the minimum and maximum elevation above the local horizon. A single value is reported in case of sidereal tracking, as referred to the center of the FoV. The object **CZ-3B R/B** was flagged as *DECAYING* on Space-Track.org at the time of the observation. It re-entered the atmosphere on August, 9th, 2022.

| Name | NORAD ID | INTLDES | Type | RCS | Perigee [km] | Apogee [km] | Obs. Date and time [UT] | Obs. Duration [sec] | Obs. Altitude [km] | ΔRange [km] | Obs. Filters | Exposure time [sec] | Max. tracking rate [°/min] | Elevation [deg] |
|---|---|---|---|---|---|---|---|---|---|---|---|---|---|---|
| FALCON 9 R/B | 41590 | 2016-038C | Rocket Body | Large | 521 | 62231 | 2022-07-19 20:43:08 | 200 | 26500 | -614 | Lum | 1 | Sidereal | 41 |
| | | | | | | | 2022-07-19 20:48:32 | 1198 | 24180 | -3924 | Lum | 1 | 0.3 | 41 - 42 |
| | | | | | | | 2022-08-05 19:24:13 | 1112 | 9500 | -4044 | g, r | 2 | 2 | 18 - 33 |
| FALCON 9 R/B | 42433 | 2017-017B | Rocket Body | Large | 200 | 30573 | 2022-07-19 19:55:17 | 1088 | 13400 | -3771 | r | 1 | 0.9 | 44 - 46 |
| LARES 2 | 53105 | 2022-080A | Payload | Medium | 5890 | 5903 | 2022-07-19 20:17:38 | 803 | 5900 | 300 | Lum | 5 | 3 | 52 - 61 |
| CZ-3B R/B | 48809 | 2021-047B | Rocket Body | Large | - | - | 2022-07-26 19:34:46 | 14 | 2300 | - | Lum | 3 | Sidereal | 25 |
| | | | | | | | 2022-07-26 19:40:23 | 181 | 2900 | 40 | g, r | 2 | 6 | 43 - 52 |
| POPACS 2 | 39269 | 2013-055E | Payload | Small | 324 | 1224 | 2022-07-19 21:47:18 | 314 | 1160 | 327 | Lum | 5 | 16 | 32 - 48 |
| IRIDIUM 33 DEB | 34492 | 1997-051GH | Debris | Small | 720 | 1133 | 2022-08-05 20:06:39 | 300 | 750 | -1436 | g, r | 3 | 30 | 10 - 74 |
| COSMOS 2251 DEB | 33821 | 1993-036BN | Debris | Small | 538 | 703 | 2022-08-05 20:28:01 | 129 | 542 | -700 | g, r | 5 | 33 | 19 - 59 |

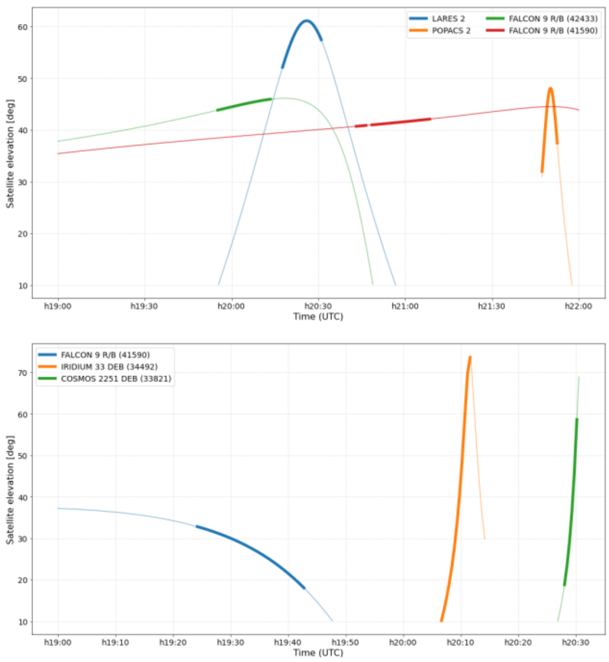


*Figure 4. Visibility curves of the targets observed on July 19th (top) and August 5th (bottom). Thick lines mark the time observation window of each object.*

The campaign was designed in order to target artificial objects over a wide range of sizes, down to ~10 cm, and altitudes between Medium (MEO) and Low Earth Orbits (LEO), down to ~500 km (Fig. 3). The second part of the campaign was run on Dec. 21st by observing 9 satellites of the GNSS system in order to characterize their multi-band (*gri*) photometry. Dates and times were chosen in order to have no interferences from the Moon glow.

A suite of scripts written in Python 3 was used to find and isolate the best targets for our purposes by querying online databases such as the CelesTrak and the Space-Track.org to retrieve their most updated Two Line Elements (TLEs), which were then used to generate the accurate ephemerides for the pointing. This code made also use of predefined Python packages such as *PyEphem* and *Astropy*. The elevation vs. time (i.e. the visibility curves) of the targets observed during the nights of July 19th and August 05th are reported in Fig. 4, along with their actual observation times, marked by the thick lines.

All the images acquired during the GRT1 pilot campaign were taken with a pixel binning of 2×2 (providing a plate scale of 2.44″/pixel) and using Luminance (Lum) filter, or either single or alternating *gri* filters. For sidereal tracking, a minimum exposure time of 1 sec was adopted in order to guarantee a good signal-to-noise for the stars in the fields (SNR ~ 25 for stars with magnitude $r \sim 10$), necessary for the differential photometry procedure used to measure the target magnitudes. For custom, non-sidereal tracking rates, a variable exposure time between 1 to 5 sec was adopted in order to guarantee a minimum SNR ~ 5, depending on the apparent brightness of the target. The images were first reduced using the proper calibration files and standard procedures (dark and bias subtraction, flat fielding correction) and aligned by using the software Tycho Tracker v.9.4.2. The frames containing the satellite streaks were finally analysed with the same software using a proper rectangular or circular aperture, according to the used tracking rate (Fig. 10).

Images taken with sidereal tracking eventually generate a measure of the apparent magnitude of the target, physically calibrated by means of the differential photometry with the known stars in the field, hence used as references for converting instrumental into apparent magnitudes. For this procedure, a minimum of 20 reference stars with $0.5 \leq B\text{-}V \leq 0.7$ were selected for each target, including stars with magnitudes up to a value of 12. The catalogue of magnitudes used for the reference stars is ATLAS one [5, 6]. For custom tracking rates, Tycho Tracker was used to extract the uncalibrated, *instrumental magnitudes* $M_{uncorr}$ of the targets. These values were then corrected for the atmospheric extinction effect, a function of both target elevation *elev* and filter wavelength $\lambda$. The magnitude correcting term $\delta M_{atm}$ was calculated as:

$$\delta M_{atm}(\lambda, \mathrm{elev}) = -\mathrm{k}(\lambda) \cdot Airmass(elev) \qquad (1)$$

Where k(λ) is the extinction coefficient, whose typical values for GAL Hassin were estimated for the different filters by using specifically acquired images. The values of the adopted model for k(λ) are reported in Table 2.

*Table 2 – Estimated values for k(λ), used in (1).*

| Filter | Wavelength [nm] | k(λ) [mag/airmass] |
|---|---|---|
| g | 400-550 | 0.22 |
| r | 550-700 | 0.18 |
| i | 700-830 | 0.24 |
| Lum | 400-700 | 0.21 |

Apparent and instrumental magnitudes were additionally corrected for the brightness change of the target due to its range variations during the observing time. Whereas this effect is small (but not negligible) for observations run with sidereal tracking – as the observation time is limited by the time taken by the target to cross the FoV – the range correction may be significant for observing times of several minutes. The magnitude correcting term $\delta M_{dist}$ for the variation of the range $D$ was calculated as:

$$\delta M_{dist}(\mathrm{D}) = -5\, log_{10}\left(\frac{D}{D_{min}}\right) \qquad (2)$$

Where $D_{min}$ is the minimum distance of the target from the observer during its observations. The final, corrected magnitudes values $M_{corr}$ were then computed as:

$$M_{corr} = M_{uncorr} + \delta M_{atm} + \delta M_{dist} \qquad (3)$$

All corrections were calculated and implemented for each observation set by means of a set of specifically developed Python 3 scripts. The corrected apparent and instrumental magnitudes were eventually used for the final analysis on rotation period measure, periodic colour variations and median colours estimate, as reported in the following sections. For the period analysis and phase folding, the Tycho Tracker period search tool plus the Python *gatspy* LombScargleFast algorithms were used.

## 4 RESULTS

In this section the targets observed for the GRT1 pilot campaign run in summer 2022 are described along with the results and outcomes obtained from their photometric analysis.

### 4.1 POPACS 2 and LARES 2

As a first test, during the same night of July 19th we observed two spherical, passive satellites, taken as examples of targets with a simple geometry and hence low intrinsic brightness variations: the Polar Orbiting Passive Atmospheric Calibration Sphere (POPACS 2) and the new LAser RElativity Satellite (LARES 2).

POPACS 2 is one of three 10-cm hollow aluminium white painted spheres, launched in 2013 on elliptical, polar orbits with the scientific goal of monitoring the density variations of the upper atmosphere (Fig. 5 – left). The observation of POPACS 2 was mainly used to obtain a first estimate of the minimum scatter associated with the GRT1 magnitude measurements and to test the ability of the GRT1 to observe small, fast satellites.

*Figure 5. Left: The three 10-cm POPACS spherical nanosatellites. Right: the LARES 2 spherical satellite.*

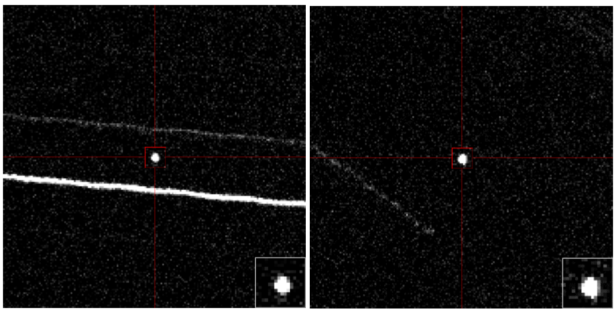

*Figure 6. POPACS 2 (left) and LARES 2 (right) as observed in a single frame of the GRT1, using an exposure time of 5 sec and tracking on the targets, with respective maximum rates of 16°/min and 3°/min.*

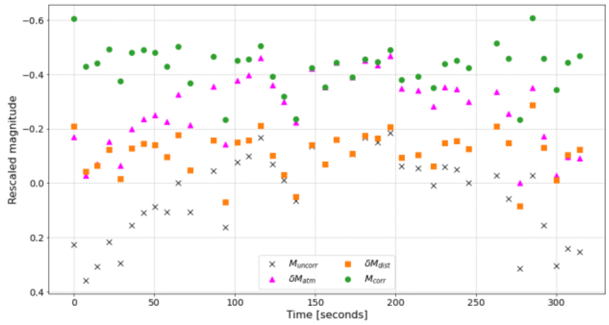


*Figure 7. The POPACS 2 raw magnitudes (black crosses), corrected for atmospheric extinction (magenta), range variation (orange) and by including both correcting terms (in green). Magnitudes have been rescaled around zero by subtracting the median value of the uncorrected magnitudes.*

The target was observed for 5 minutes when it was at an altitude ~ 1200 km, with a maximum tracking rate of 16°/min. It was detected in the single frames with a SNR ~ 70 (Fig. 6 – left). The magnitudes values measured for POPACS 2 were *instrumental*, and they were corrected both for atmospheric extinction and range variation effects, generating an almost flat light curve with an intrinsic RMS ~ 0.08 mag (green points of Fig. 7).

LARES 2 is a 42-cm nickel sphere containing 303 cube corner retroreflectors (Fig. 5 – right). It was launched on July 2022 with the goal of measuring the tiny effects of relativistic frame-dragging with unprecedented accuracy. The target was observed for 13 minutes at an altitude around 5900 km and with a maximum rate of 3°/min. It was detected with a SNR ~ 40 (Fig. 6 – right). The instrumental magnitudes extracted for LARES 2 were also corrected both for atmospheric extinction and range variation effects, generating a light curve with an intrinsic RMS ~ 0.26 mag (Fig. 8).

As a further check, the POPACS 2 and LARES 2 corrected light curves have been compared with the simple models of *diffuse* and *specular spheres*, as described in [5]. In these models, the satellite brightness should depend upon its phase angle $\alpha$ as:

$$F_1(\alpha) = \frac{2}{3\,\pi^2}\,[(\pi - \alpha)cos\alpha + sin\alpha] \qquad (4)$$

for a diffuse sphere, and:

$$F_2(\alpha) = \frac{1}{4\pi} \qquad (5)$$

for a specular sphere.

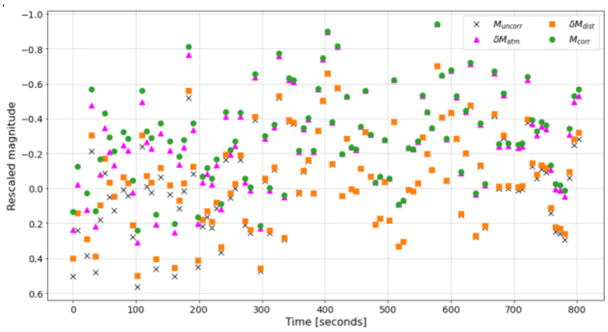


*Figure 8. The LARES 2 raw and corrected magnitudes.*

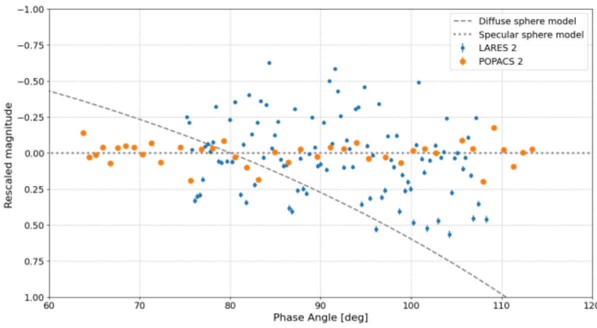


*Figure 9. The POPACS 2 and LARES 2 corrected magnitude plotted against their phase angles. Overlaid in grey are the diffuse (dashed line) and specular (dotted line) sphere models, for comparison. POPACS 2 magnitudes appear to be almost independent from the phase angle, as expected for a perfect specular sphere.*

In Fig. 9, the corrected magnitudes of the two spherical satellites are plotted against their phase angle, together with the logarithm of $F_1$ from (4) and $F_2$ from (5). All curves and points have been rescaled to zero for phase angle = 80 deg. This analysis seems to demonstrate that POPACS 2 is an almost perfect specular sphere, as expected from its extremely regular and reflective surface. On the other hand, LARES 2 exhibits a brightness behaviour which lies between the two simplistic models, especially for $\alpha > 100°$. This might be the effect of its retroreflectors which prevent LARES 2 behaving like a perfectly regular, homogenously reflecting spherical surface.

### 4.2 FALCON 9 R/B (41590)

As a second test, on July 19th we observed a large and irregular object with two different tracking rates, in order to check the consistency of the results on its variability coming from the two approaches. For this purpose, we targeted the object FALCON 9 R/B (NORAD ID: 41590): the cylindrical booster of the FALCON 9 second stage, with a size of about 3.5 × 8 m and an empty mass of ~ 4000 Kg. We observed the rocket body with a first set of images taken at sidereal rate and the second one by tracking the target, at ~ 0.3°/min (Fig. 10). In both cases the Lum filter was used, and the target was detected with a SNR ~ 110.

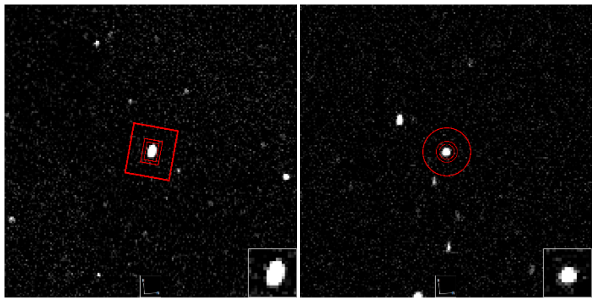

*Figure 10. The FALCON 9 R/B (41590) as observed with 1 sec exposure time in sidereal tracking (left) and object tracking (right). In red are the corresponding apertures used for computing the magnitudes from the two sets.*

The first set generated already calibrated magnitudes thanks to the differential photometry technique, as described in Sect. 3, whereas instrumental magnitudes were extracted for the second one. With sidereal tracking, observations of a moving target are limited by the time the object takes to cross the FoV. For this reason, a maximum of about 60 frames with 1 sec exposure time could be taken for the first set, for a total of 3.3 min. For the second set, with target tracking, the observations time window could be expanded up to ~20 min, with a total of about 350 frames of 1 sec exposure. The period analysis of the two sets generated a clear identification of a rotation period P ~ 86.8 sec. Specifically, for the first set P = 86.81 and amplitude A = 1.60 mag was obtained. The second, much denser set generated P = 86.82 and A = 1.66 mag. The two folded light curves are reported in Fig. 12, along with their best Fourier fits (10th degree series).

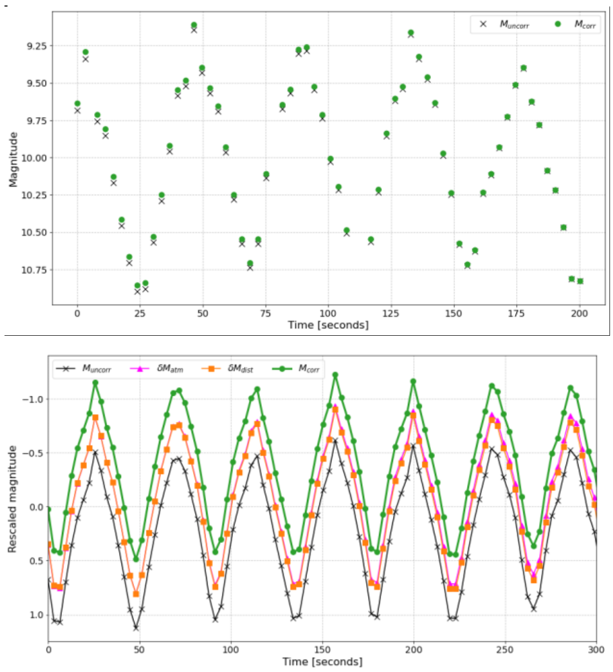


*Figure 11. The complete light curve extracted for the FALCON 9 R/B (41590) with sidereal tracking (top) and the first 300 sec with target tracking (bottom). Only $\delta M_{dist}$ correction term was applied to the first data set.*

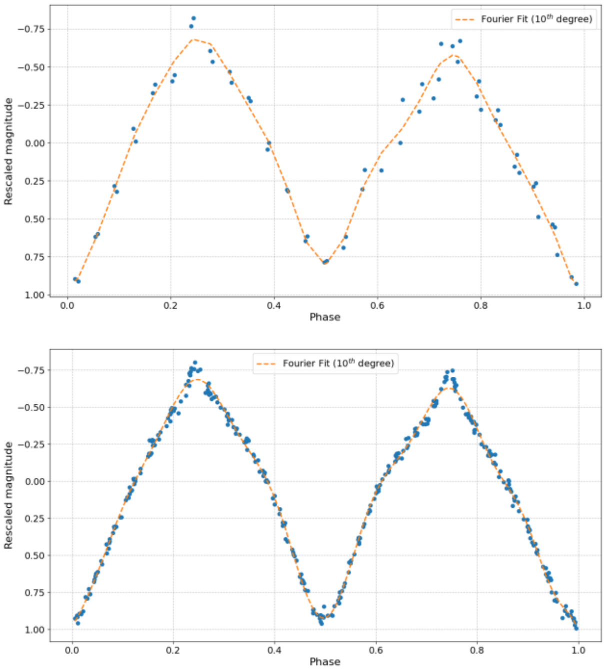


*Figure 12. The phase plots of the FALCON 9 R/B (41590) light curves observed in sidereal tracking (top) and object tracking (bottom). Both curves have been rescaled to zero by subtracting the median magnitudes. Dashed lines are the 10$^{th}$ degree Fourier series fit, with residual RMS of 0.073 mag and 0.034 mag, respectively.*

These results validate the perfect consistency in period (within 0.01 sec) and amplitude (within 0.06 mag) determination achieved either with sidereal or object tracking methods. Of course, because of its time limitation, the observation in sidereal tracking generated a much sparser dataset, which prevented to delineate the accurate profile of the FALCON 9 booster rotation light curves, as can be appreciated by comparing the details of the folded light curves shown in Fig. 12.

### 4.3 FALCON 9 R/B (42433)

The booster FALCON 9 R/B (42433) was observed for about 18 min in *Sloan-r* filter at the beginning of the night of July 19$^{th}$, with a tracking rate ~ 0.9°/min. With an exposure time of 1 sec, the object was detected with a SNR ~ 450. Fig. 13 shows the rescaled raw and corrected magnitudes, and illustrates how the instrumental, uncorrected magnitude considerably rose in the observation window. This effect was actually related to the *negative* variation in range of the booster, which steadily moved from a distance of 17000 km to 13000 km, generating a constant brightness rise of ~ 0.5 mag. In fact, Fig. 13 also shows how the final, corrected magnitude is flattened especially by the $\delta Mag_{dist}$ term (orange points). The period analysis clearly identified a periodicity of P = 548.16 sec and amplitude A = 1.02 mag (Fig. 14). The residuals of the Fourier fitting have an RMS of 0.035 mag.

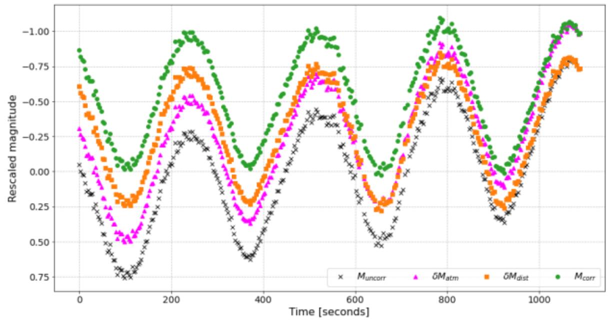


*Figure 13. Rescaled magnitudes of FALCON 9 R/B (42433). It is evident how the (steadily rising) uncorrected magnitude gets flattened especially by the $\delta Mag_{dist}$ term.*

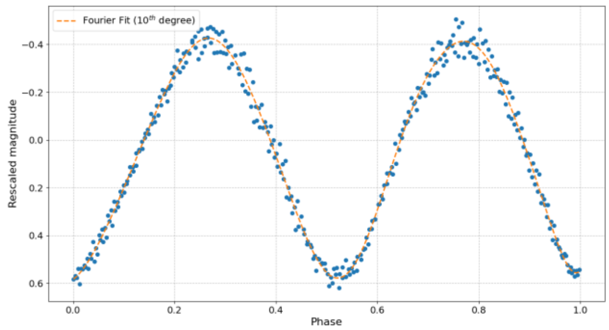


*Figure 14. Folded phase plot of FALCON 9 R/B (42433) light curve, including its Fourier fit series of 10$^{th}$ degree.*

The folded light curve of the FALCON 9 (42433) appears to be shaped differently from the FALCON 9 (41590) one, possibly indicating different observation geometries and illumination conditions for the two boosters. However, the photometric analysis of the two FALCON 9 boosters indicates that both cylinders are probably regularly rotating around their short axis.

### 4.4 *g/r* observation of FALCON 9 R/B (41590)

We re-observed the FALCON 9 R/B (41590) during the night of August, 5$^{th}$, tracking the object at a maximum of 2°/min, using 2 sec exposure time and *alternating* the *g* and *r* filters in order to characterize the target with a quasi-simultaneous dual-band photometry. The debris was detected with a SNR ~ 150 in *g* and SNR ~ 250 in *r*. The instrumental magnitudes were corrected as usual, using the appropriate k(λ) for each filter, as reported in Tab. 1. Period analysis was then performed using both magnitudes, jointed after rescaling both to zero. The analysis returned again a P = 86.81 sec: perfectly consistent with our findings reported in Sect. 4.2 for the observations in Lum filter.

We then generated the phase plot by folding *g* and *r* series with the same period, but *without* the applied magnitude offset in order to inspect any variation of the *g-r* colour with the rotation phase. The phase plots of *g* and *r* series are shown in Fig. 15.

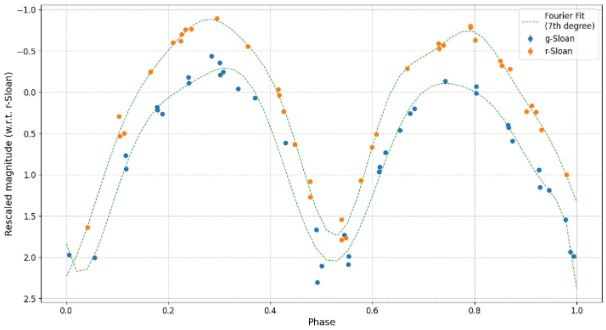


*Figure 15. Phase plot of the FALCON 9 (41590) for r and g magnitudes. Green lines are the Fourier fit (7$^{th}$ degree). Associated magnitude errorbars are less than 0.005 mag, and are smaller than the marker symbols.*

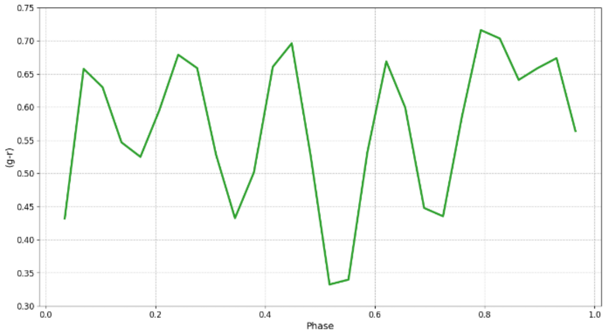


*Figure 16. The variation of the g-r colour of the FALCON 9 (41590) with its rotation phase. We found a clear wiggle, symmetric pattern around a median value g-r ~ 0.60, possibly indicating that different materials of the debris are exposed/illuminated during its rotation.*

The two respective Fourier fitting series of 7$^{th}$ order have been subtracted in order to inspect if and how the *g-r* colour correlated with the phase. We found a median value of *g-r* ~ 0.6, but with a wiggle, symmetric pattern which may be caused by different material (and hence coloured surfaces) which are illuminated and become visible with the rotation of the cylindric rocket body (Fig. 16). Specifically, we found the booster seems to appear *bluer* (*g-r* ~ 0.3) during its minimum brightness, and *redder* (*g-r* ~ 0.7) during its maxima.

### 4.5 CZ-3B R/B (48809)

During the night of July, 26$^{th}$, 2022 we observed the object CZ-3B R/B (NORAD ID: 48809), a stage of the Chinese orbital launch vehicle Long March 3B. This target was selected as it was announced in imminent *decay* by Space-Track.org (DECAY_EPOCH: 2022-08-06). The booster actually reentered on 2022/08/09.

The first observing session targeted the object in sidereal tracking, with the aim of measuring its astrometry.

*Figure 17. The three streaks left by CZ-3B in the three consecutive GRT1 images of 3 sec exposure time. Green crosses mark the positions of the measured astrometry, covering a distance of ~1.2 deg over ~15 sec. The booster was moving from the top-right to the bottom-left corner.*

Thanks to the large FoV of the GRT1, we managed to obtain the images of three (entire and partial) streaks within the same field despite the high rate of the target (~6°/min). Hence, we could measure the accurate astrometry of the beginning of each streak, covering a total arc of about 1.2 deg on a 15 seconds time window (Fig. 17). These observations demonstrated the possibility of using our GRT1 in supporting projects that require accurate astrometry, like prediction of debris *reentry corridor*, satellites *collision avoidance*, etc.

On the same night, CZ-3B R/B was also targeted for dual *g/r* filters photometry, in order to estimate both its rotation period and *g-r* colour properties. We acquired image with 2 sec exposure times, reaching SNR ~ 1000 in *g* and SNR ~ 1200 in *r*. Because of a technical issue on the filter wheels, the observations had to be aborted after about 3 min and a total of only 20 frames.

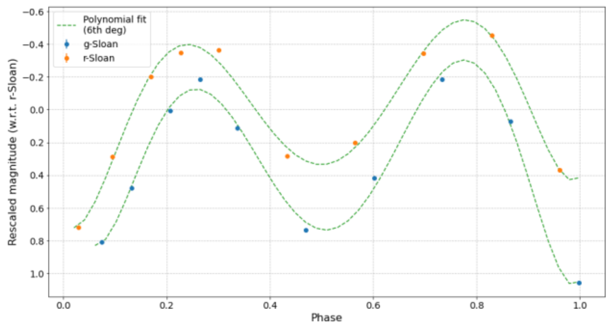


*Figure 18. Phase plot of the CZ-3B (48809) for r and g magnitudes. Green lines are a 6$^{th}$ degree polynomial fit.*

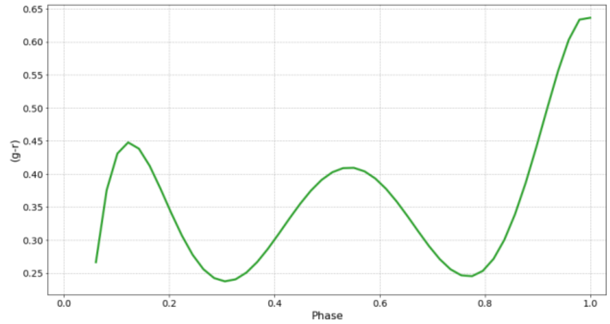


*Figure 19. The variation of the g-r colour of the CZ-3B (48809) with its rotation phase. We found a colour variation of about ±0.1 mag around a median g-r ~ 0.35, with the object appearing redder at the minimum of its brightness, and bluer at the maximum.*

The corrected and *combined* *g* and *r* instrumental magnitudes were then used for the period analysis, obtaining a P = 150.2 sec, which was used to fold both the *g* and *r* series shown in Fig. 18. The two respective fitting polynomials of 6$^{th}$ degree were then subtracted in order to obtain the variation of the *g-r* colour with the phase. We found a median value of *g-r* ~ 0.35, with a varying, symmetric pattern of ±0.10 mag (Fig. 19). Specifically, we found the booster appeared *bluer* (*g-r* ~ 0.25) during its maximum brightness, and *redder* (*g-r* ~ 0.40) during its minima.

## 4.6 IRIDIUM 33 DEB (34492) and COSMOS 2251 DEB (33821)

As final targets of the GRT1 summer 2022 pilot campaign, two small debris generated during the 2009 satellite collision event and orbiting at an altitude less than 1000 km were observed. Specifically, we targeted IRIDIUM 33 DEB (34492) and COSMOS 2251 DEB (33821) for a quasi-simultaneous dual-filter (*g/r)* characterization. The IRIDIUM 33 DEB was tracked at a maximum rate of 30°/min and was observed with 3 sec exposure time in both filters. It was detected at SNR ~ 5 in *g* and SNR ~ 8 in *r*. The COSMOS 2251 DEB was tracked at 33°/min at maximum and observed with exposure times of 5 sec. It was detected with SNR ~ 20 in *g* and SNR ~ 30 in *r*.

The instrumental magnitudes were reduced as usual, and the closest in time (*g, r*) pairs were subtracted in order to construct the curve of the *g-r* colour variation with time (Fig. 20 and 21). No period analysis was performed. However, from Fig. 20 there seems to be present a periodic variation in the brightness *and* in the colour of the IRIDIUM 33 debris, with a period ~ 150 sec. The relatively low SNR and the short time coverage do not allow to draw any conclusive statement on this aspect. Overall, for the object was measured a median *g-r* ~ 0.43.

The COSMOS 2251 debris showed a smoother light and colour curves, with a median *g-r* ~ 0.45.

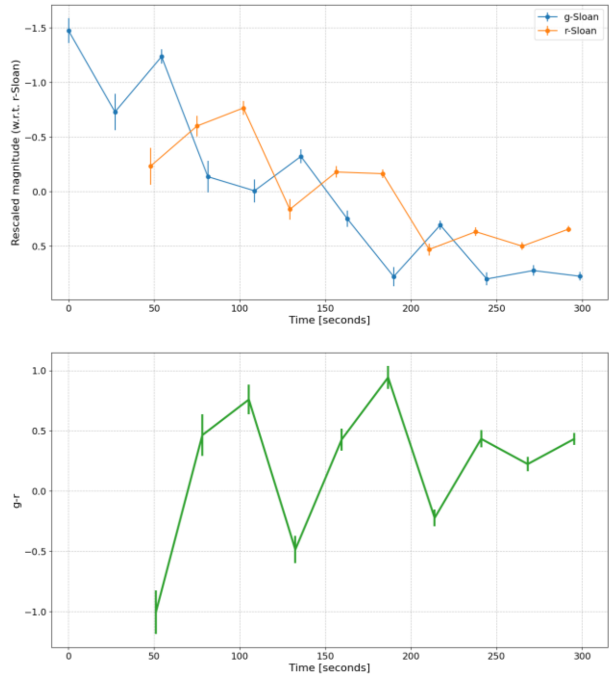


*Figure 20. Top: The corrected, quasi-simultaneous g and r magnitudes of the debris IRIDIUM 33 (34492), observed for about 5 min. Bottom: The observed g-r colour variation vs. the time elapsed from the first point.*

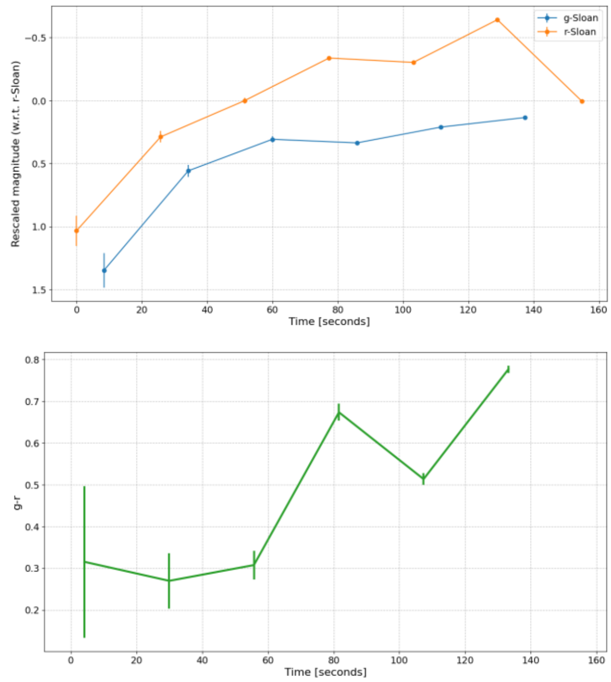


*Figure 21. Top: The corrected, quasi-simultaneous g and r magnitudes of the debris* COSMOS 2251 (33821*), observed for about 2.5 min. Bottom: The observed g-r colour variation vs. the time elapsed from the first point.*

Table 3. *Properties of the 9 GNSS satellites observed by the GRT1 on December, 21st, 2022. The observations were carried out by alternating gri filters, with the goal of characterize the specific colour of each GNSS satellite class.*

| ID | INTLDES | Constellation | Obs. Time | Elevation [deg] | Elong. [deg] | g-r | r-i | g-i |
|---|---|---|---|---|---|---|---|---|
| E26 | 2015-017A | GALILEO-2 | 19:50:30 | 78 | 146 | $0.01 \pm 0.15$ | $0.20 \pm 0.12$ | $0.21 \pm 0.17$ |
| C27 | 2018-003A | Beidou-3 M3 | 20:06:00 | 57 | 145 | $0.38 \pm 0.12$ | $0.23 \pm 0.12$ | $0.61 \pm 0.14$ |
| G18 | 2019-056A | GPS – BLOCK IIIA | 20:33:00 | 80 | 150 | $0.19 \pm 0.10$ | $0.18 \pm 0.09$ | $0.37 \pm 0.08$ |
| R18 | 2014-012A | GLONASS-M | 20:45:00 | 58 | 130 | $0.40 \pm 0.08$ | $0.25 \pm 0.06$ | $0.65 \pm 0.09$ |
| C30 | 2018-029B | Beidou-3 M8 | 21:14:00 | 68 | 135 | $0.24 \pm 0.09$ | $0.26 \pm 0.10$ | $0.50 \pm 0.11$ |
| G26 | 2015-013A | GPS – BLOCK IIF | 21:30:00 | 69 | 148 | $0.57 \pm 0.08$ | $0.51 \pm 0.07$ | $1.08 \pm 0.09$ |
| E31 | 2017-079D | GALILEO-2 | 21:47:30 | 65 | 135 | $0.23 \pm 0.11$ | $0.26 \pm 0.10$ | $0.49 \pm 0.11$ |
| R19 | 2007-052A | GLONASS-M | 22:00:00 | 55 | 127 | $0.45 \pm 0.08$ | $0.34 \pm 0.07$ | $0.79 \pm 0.08$ |
| E33 | 2018-060B | GALILEO-2 | 22:10:00 | 71 | 144 | $0.19 \pm 0.12$ | $0.07 \pm 0.13$ | $0.25 \pm 0.13$ |

## 5 *gri* observations of GNSS satellites

On December, 21st, 2022 the second part of the GRT1 pilot campaign was carried out on a set of GNSS satellites belonging to different constellations (Fig. 24). In 2021 the GRT1 has been used for a similar campaign aimed at characterizing the r-Sloan photometry of OneWeb *LEO* satellites with the goal of modelling their brightness under different conditions and hence reducing their light pollution in 2nd generation satellites. The details of this study are fully described in a forthcoming publication [8].

For the 2022 campaign, following the strategy discussed in [9], the GNSS targets were observed using alternating *g-r-i* filters to measure their colours and intrinsic scatters, and to inspect if the different GNSS constellations appear *clustered* in colour – colour spaces (as expected by assuming specific materials and reflecting surfaces for each category of satellite).

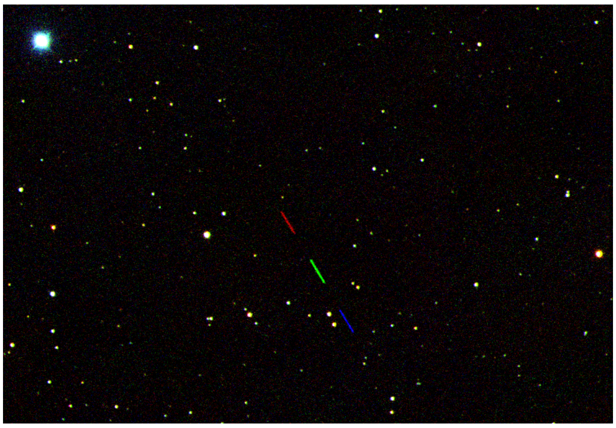

*Figure 22. An rgi composite GRT1 image showing the three streaks left by the satellite E33 over a stellar field in the three consecutive filters Sloan-g (blue), Sloan-r (green) and Sloan-i (red). The three streaks are separated in time by 3 seconds.*

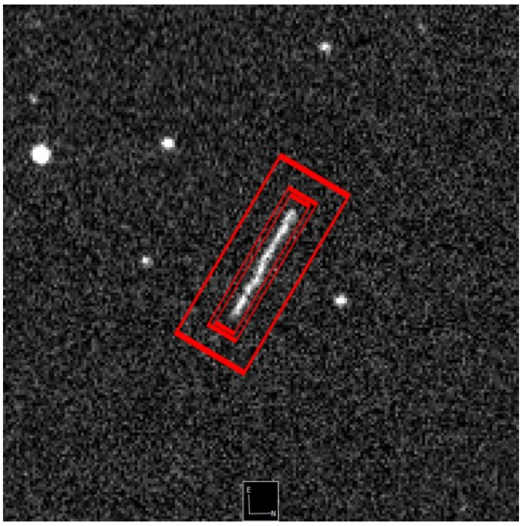

*Figure 23. An example of the rectangular apertures used in Tycho Tracker to measure the magnitude of the satellites' streaks. A fixed, circular aperture was instead used for the comparison stars.*

In order to observe the satellites under similar illumination conditions, the targets were selected within a solar elongation range of $130° \leq Elong. \leq 150°$. In addition, targets were observed only if and when reaching elevations of $Elev. \geq 60°$ with the goal of minimising the chromatic atmospheric extinction effects (Tab. 3).

The accurate ephemerides of each satellite were calculated via a series of Python scripts and of the most updated TLEs provided by the CeleStrak website. Once on position, the telescope started acquiring a continuous series of 3 sec images alternating the three *gri* filters, until the satellite had completely crossed the field. This approach enabled the acquisition of multiple streaks in the three different filters for a same pointing (Fig. 22). Each set of images taken with the same filter was then


*Figure 24. Example pictorial representations of the GNSS satellites observed in the GRT1 space debris pilot campaign.*

reduced, aligned and plate solved with the Tycho Tracker software, following the standard procedures. The same software was finally used to measure the magnitudes of the streaks by using properly sized rectangular apertures (Fig. 23). Since the observations were run in sidereal tracking mode, the aforementioned *differential photometry* technique was adopted, always using a minimum of 20 comparison stars, isolated and with solar colours 0.5 ≤ B-V ≤ 0.7.

The satellites colour – colour plots *r-i* vs *g-r* and *r-i* vs *g-i* are shown in Fig. 25. The reported results, although still preliminary because of the small samples sizes, indeed appear to point toward a *clustering* of the satellites belonging to the same constellation within a small and well-defined area in the colour – colour spaces. Thus, supporting the results obtained for GEO satellites by using Johnson bands in [9]. The only exceptions are the two GPS satellites 2019-056A and 2015-013A, because of their extremely different colours. However, these two objects belong to two different generations (IIF and IIIA) of GPS satellites, characterized by different shapes and external colours. In fact, as can be seen in Fig. 24, the GPS-IIF generation has a much redder spacecraft, consistent with our findings and the colour discrepancy found from the IIIA-gen GPS. Finally, the streaks of the observed GNSS satellites were also used to estimate the accuracy and possible bias in the GRT1 reported time, as illustrated in [10]. The astrometry was measured on the initial point of each streak (as in Fig. 17) and it was then analysed via the "*Check GNSS astrometry*" online tool provided by the *ProjectPluto* webpage. Via this online software one can check the *along-track* and *cross-track* residuals, respectively measuring the *timing* and the *astrometric* (positioning) errors. The outcome of the analysis is reported in Fig. 26, where the different GNSS groups are separated by the different colours and symbols. Overall, we did not find any significant discrepancies in using the four different GNSS groups, and we could estimate a global residual in the *along*- and *cross-track* of:

**Avg along-track (timing)**: +0.13 ± 0.08 seconds
**Avg. cross-track**: -0.10 ± 1.42 arcsec

This pointed toward a systematic *positive bias* in the timing of the GRT1 observations, i.e., the times reported in the astrometry are *earlier* than the positions of the GPS satellites would indicate. This is a typical effect caused e.g., by the tiny – but still measurable – delay between when the time is written into the file header and when the

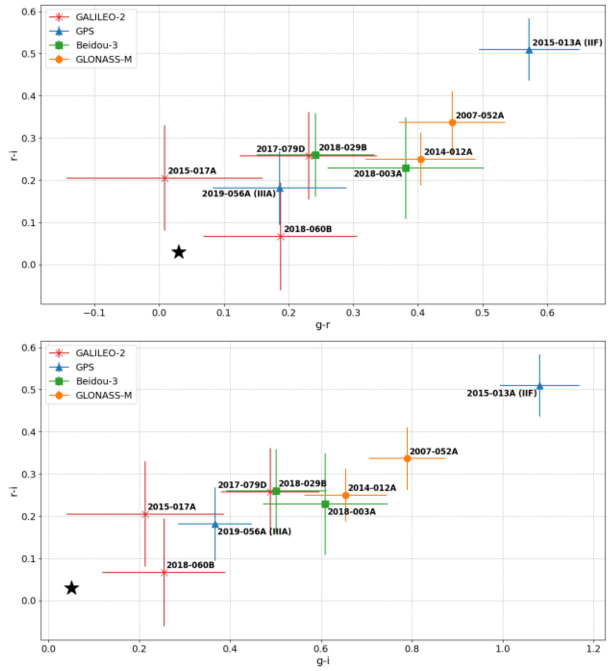


*Figure 25. The colour – colour plots of the observed GNSS satellites. The colours of the different symbols identify satellites belonging to different constellations. The black star marks the position of the Sun in the plots. Top: r-i vs g-r. Bottom: r-i vs g-i.*

camera shutter actually opens and starts recording the position of the satellite. Once such a timing bias is robustly estimated, it can be corrected for by systematically subtracting it from the astrometric measurements.

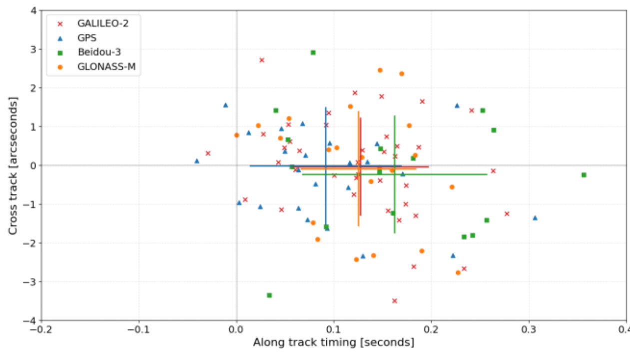


*Figure 26. The along track and cross track residuals, providing respectively a measure of the GRT1* ***timing*** *and* ***positioning*** *error, obtained using different GNSS constellations. Crosses positions and sizes refer to the mean and scatter values of each group.*

## 6 CONCLUSIONS

The presented work tested and validated some observational strategies, hardware facilities and data analysis techniques for the accurate observations and characterization of artificial satellites and space debris. They have been tested on the Galhassin Robotic Telescope 1 (GRT1), which was validated as being an effective facility to observe, characterize and track artificial objects down to an altitude of about 500 km and with an RCS < 0.1 $m^2$. In particular, thanks to its large FoV, the fast and accurate tracking mount and the GPS time synchronization facility, we verified that:

1. The GRT1 is able to provide accurate astrometry of fast objects with a time accuracy of ~ 0.1 sec, key to provide services such as collision avoidance, reentry & decay corridor determination, etc.
2. The photometric measurements of the GRT1 can reach an accuracy of about 0.035 mag.
3. The GRT1 mount provides extremely accurate tracking for both sidereal and custom rates up to 2°/sec (or 120°/min), key to track low altitude targets for the longest possible time windows simply using their up-to-date TLEs as input.
4. Due to continuous images acquisition, satellites and debris light curves can be sampled with frequencies $\nu \sim 0.5$ Hz for single filter observations (the overhead time of ~ 2 sec is dominated by the PC download time), and $\nu \sim 0.1$ Hz for alternating filters mode (~3.5 and ~11 sec overheads dominated by the time needed by the filter wheel to go to the next filter and to restart the filter series, respectively).
5. Light curves and multiband magnitudes can be measured by differential photometry techniques for objects remaining within the sensor area (82×82 arcmin) for a sufficiently long time (corresponding e.g. to ~180 sec for GPS satellites at 20000 km altitude).
6. The custom tracking guaranteed by the mount gives access to a *quasi-simultaneous* multi-band photometry for long times (entire visibility window) even for very fast objects, using their instrumental magnitudes. Such a quantity, although not physically calibrated, after being corrected for atmospheric extinction and range variation effects can be still used to accurately determine the rotation periods, colour indices and how the reflectivity properties (and hence material) of the targets change with their rotation phase.
7. Photometric tests performed on LARES 2 and POPACS 2 objects verified the actual absence of periodic variations in the light curve, as expected from the spherical geometry of those objects. In addition, this result also demostrated the photometric accuracy reached by the GRT1 even for decimetre-scale objects such as POPACS 2.
8. The observations with alternating *gri* filters can potentially help in *classifying* debris and satellites based on their external materials according to their positions within a colour – colour space. This was successfully tested on a small set of GNSS satellites belonging to different constellations groups, but it can be expanded and potentiated once a proper, preliminary calibration on larger and representative target sets is performed. See also the analysis and results from [9] for GEO satellites.

The GRT1 performances described in this paper are expected to be further improved by installing a sCMOS camera in place of the current CCD: the gain in sensitivity and noise reduction would greatly improve the SNR of the targets observed at a given exposure time, and hence the quality of their photometric characterization. In addition, sCMOS can reach much faster time samplings of the light curves and hence a more accurate period determination, which would be extremely useful for fast-rotating, smaller debris.

The results of the GRT1 pilot observations discussed in this work will be of great help and possibly be (partially or entirely) used and implemented for the future, upcoming generation of 1-m class wide-field telescopes which are being installed within the Madonie regional park, in Sicily: the Wide-field Mufara Telescope (WMT) and the ESA NEOSTEL "Flyeye" telescope. Such an array will be the first of its kind in Europe, and will open new perspectives in the research, characterization and coordinated observations of fast, artificial objects and NEOs.

## 7 REFERENCES


1. Di Cecco, A.; Perozzi, E.; Marzo, C., et al., (2019). *Analysis of Italian sites for NEO and Space Debris observations with the ESA Flyeye telescope*. 1st NEO and Debris Detection Conference: 6 p., Darmstadt (Germany): ESA Space Safety Programme Office.

2. Cibin, L.; Chiarini, M.; Bernardi, F.; Ragazzoni, R.; Salinari, P. (2016). *NEOSTEL: the telescope detail design program for the ESA optical ground network dedicated to NEO discovery and tracking*. 2016MmSAI..87..197C (https://ui.adsabs.harvard.edu/abs/2016MmSAI..87..197C/abstract).

3. Marchiori, G.; Tordi, M.; Ghedin, L. et al. (2022). *NEOSTEL: the first innovative observatory for the FlyEye Telescopes*, 2022SPIE12182E..4KM (https://ui.adsabs.harvard.edu/link_gateway/2022SPIE12182E..4KM/doi:10.1117/12.2630258).

4. WMT – 1m Wide Field Mufara Telescope: https://www.officinastellare.com/projects/wmt-1m-wide-field-mufara-telescope/

5. Tonry, J. L., Denneau, L., Flewelling, H. et al. (2018). *The atlas all-sky stellar reference catalog*. The Astrophysical Journal, 867(2). doi:10.3847/1538-4357/aae386.

6. Kostov, A., & Bonev, T. (2017). *Transformation of pan-starrs1 gri to Stetson bvri magnitudes. photometry of small bodies observations*. Bulgarian Astrophysical Journal, 28. arXiv:1706.06147.

7. Silha, J., Zigo, M., Hrobar, T., Jevcak, P. (2021). *Light curves application to space debris characterization and classification*. 8th European Conference on Space Debris, 20 April 2021 - 23 April 2021, Darmstadt, Germany, published by ESA Space Debris Office.

8. Littoriano, G.; Colombo, C., Nastasi, A.; Falco, C. (2023). *Brightness modelling of spacecraft apparent brightness. A study on OneWeb constellation satellites*. Submitted.

9. Di Cecco, A.; Buzzoni, A.; Mochi, M. et al. (2023). *Geo Satellites' Manufacturing Markers From Photometric Colors.* Proc. of the 2nd ESA NEO and DEBRIS DETECTION CONFERENCE, 24-26 January 2023.

10. Gray, Bill. *Calibrating timing of astronomical images using navigation satellites*: https://projectpluto.com/gps_expl.htm